A smoothed particle hydrodynamics algorithm for multigrain dust with separate sets of particles

Daniel Mentiplay, Daniel J. Price, Christophe Pinte, Guillaume Laibe

Monthly Notices of the ROYAL ASTRONOMICAL SOCIETY

MNRAS **499,** 3806–3818 (2020) doi:10.1093/mnras/staa3171
Advance Access publication 2020 October 15

A smoothed particle hydrodynamics algorithm for multigrain dust with separate sets of particles

Daniel Mentiplay [1]★ Daniel J. Price [1] Christophe Pinte [1,2] and Guillaume Laibe[3]

[1]*School of Physics and Astronomy, Monash University, Clayton, VIC 3800, Australia*
[2]*CNRS, IPAG, University Grenoble Alpes, F-38000 Grenoble, France*
[3]*École normale supérieure de Lyon, CRAL, UMR CNRS 5574, Université de Lyon, 46 Allée d'Italie, F-69364 Lyon Cedex 07, France*

Accepted 2020 October 10. Received 2020 October 9; in original form 2020 August 9

ABSTRACT

We present a method for simulating the dynamics of a mixture of gas and multiple species of large Stokes number dust grains, typical of evolved protoplanetary discs and debris discs. The method improves upon earlier methods, in which only a single grain size could be represented, by capturing the differential backreaction of multiple dust species on the gas. This effect is greater for large dust-to-gas ratios that may be expected in the later stages of the protoplanetary disc life. We benchmark the method against analytic solutions for linear waves, drag, and shocks in dust–gas mixtures, and radial drift in a protoplanetary disc showing that the method is robust and accurate.

Key words: hydrodynamics – methods: numerical – protoplanetary discs.

1 INTRODUCTION

In order to interpret dust continuum emission, for example, in ALMA observations showing gaps and rings (ALMA Partnership et al. 2015; Andrews et al. 2016), we must model planet–disc interactions including multiple species. At any continuum wavelength grains of multiple sizes contribute to the observed emission. In addition, spectral index maps can put constraints on the size distribution of dust grains within gaps (Huang et al. 2018). Multispecies dust models allow us to test the underlying disc models by producing synthetic spectral index maps to compare with observations (Casassus et al. 2015; Pinte et al. 2016).

Multiwavelength observations of protoplanetary discs show that the radial extent of the dust disc scales inversely with wavelength, i.e. inversely with dust grain size (Andrews 2015). Modelling this requires dust and gas hydrodynamics with multiple dust species – one of the grand challenges in protoplanetary disc modelling (Haworth et al. 2016). In particular, it is important to capture the collective backreaction of multiple dust species on the gas (Dipierro et al. 2018). For example, small grains are well coupled to the gas and follow its inward or outward motion (Weidenschilling 1977). Larger grains drift inwards due to the differential velocity between the pressure-supported gas, and, due to conservation of angular momentum, the gas might drift outwards dragging the small grains with it (Laibe & Price 2014c).

Radiative transfer calculations offer a way to validate hydrodynamical models of protoplanetary discs by producing synthetic observations for comparison with observations. These calculations require knowledge of the distribution of many dust species from the hydrodynamical simulation. The ability to perform multiwavelength synthetic observations in single species dust–gas hydrodynamical models is limited. One option is to stack, in post-processing, multiple single dust species simulations (Dipierro et al. 2015; Mentiplay, Price & Pinte 2019). However, due to backreaction, there may be a phase difference in the location of the concentration making this procedure unreliable. For example, discs containing dust asymmetries and spiral arms around central cavities can show greater concentration at different wavelengths (Casassus et al. 2015; van der Marel et al. 2015). Previous work has suggested that the cause of these features is a (possibly unseen) companion in the cavity (Price et al. 2018b; Calcino et al. 2019; Poblete, Cuello & Cuadra 2019). Due to the potential for a phase difference in these single-species simulations, producing multiwavelength synthetic observations requires multiple dust species within the same hydrodynamical simulation.

Several groups have developed methods for simulating the hydrodynamics of dust–gas mixtures with multiple dust species with both grid and particle methods, e.g. Bai & Stone (2010a), Porth et al. (2014), Hutchison, Price & Laibe (2018), Benítez-Llambay, Krapp & Pessah (2019), Lebreuilly, Commerçon & Laibe (2019), and Li et al. (2019). The methods of Benítez-Llambay et al. (2019) and Lebreuilly et al. (2019) are limited by their use of the single fluid approach (discussed below). Bai & Stone (2010a), Porth et al. (2014), and Li et al. (2019) describe grid codes which can introduce grid-alignment issues.

Smoothed particle hydrodynamics (SPH) is a particle method for solving the equations of hydrodynamics (Monaghan 1992, 2005; Price 2012). The fluid, typically gas, is discretized on to a set of particles rather than a grid. There are two approaches to modelling of dust–gas mixtures in SPH: (i) the dust and gas are represented by separate sets of SPH particles (Monaghan & Kocharyan 1995; Laibe & Price 2012a,b). In this approach, the dust and gas SPH particles interact via a drag coupling term. In the other approach, (ii), the dust and gas are modelled by a single set of SPH particles representing the mixture (Laibe & Price 2014a,b,c; Price & Laibe 2015; Ballabio et al.

★ E-mail: daniel.mentiplay@monash.edu

2018). In this approach, the dust fraction is stored on the particles and evolved in time.

Typically, in both of these methods, an explicit time-stepping scheme is used. One problem with such schemes is that the drag time-scale can be many orders of magnitude smaller than other physically interesting time-scales, e.g. the orbital time in a protoplanetary disc. This requires taking small time-steps and is computationally inefficient. Various groups have developed implicit or semi-implicit time-stepping methods that remove the restriction of small time-steps required by explicit schemes for drag (Monaghan 1997; Laibe & Price 2012b; Lorén-Aguilar & Bate 2014, 2015; Stoyanovskaya et al. 2018).

In the description for both of these approaches (the dust as separate particles method and the single SPH fluid mixture method), the methods are applicable to a single species of dust with fixed size. Laibe & Price (2014c) and Hutchison et al. (2018) described a multiple species approach for the single SPH fluid method. Hutchison et al. (2018) derived the version using the terminal velocity approximation, and tested this in the PHANTOM SPH code (Price et al. 2018a). The single fluid approach is limited in that particles are not allowed to stream past each other as expected for large, weakly coupled grains (Laibe & Price 2014b). The methods of Benítez-Llambay et al. (2019), Lebreuilly et al. (2019), and Li et al. (2019) are based on the single fluid approach.

In this paper we extend method (i), in which dust is represented by separate sets of particles, from a single species to multiple species. We present the continuum equations to solve in Section 2.1, and the SPH discretization of those equations in Section 2.3. We describe several tests of the method, as implemented in PHANTOM, in Section 3. We discuss some of the challenges of the method in Section 4.

2 METHODS

2.1 Continuum equations for multiple dust species

We consider a mixture of gas, indexed by g, and N dust species, indexed by d_i. We neglect the finite size of the dust particles, and thus set the gas volume fraction to unity. We represent each dust species as a continuous fluid with a fixed size, s_i, and intrinsic density, ϱ_{m_i}. Then, the equations of conservation of mass for the mixture is given by

$$\frac{\partial \rho_{\mathrm{g}}}{\partial t} + \nabla \cdot (\rho_{\mathrm{g}} \boldsymbol{v}_{\mathrm{g}}) = 0, \tag{1}$$

$$\frac{\partial \rho_{\mathrm{d}_i}}{\partial t} + \nabla \cdot (\rho_{\mathrm{d}_i} \boldsymbol{v}_{\mathrm{d}_i}) = 0, \tag{2}$$

for each i in 1 to N, where ρ_{g} and $\boldsymbol{v}_{\mathrm{g}}$ are the gas density and velocity, and ρ_{d_i} and $\boldsymbol{v}_{\mathrm{d}_i}$ are the dust density and velocity.

We assume the fluids are inviscid, that the dust is pressureless, and that each dust species is homogeneous, i.e. has the same grain size, mass, and intrinsic density. The equations of conservation of momentum for the mixture are given by

$$\rho_{\mathrm{g}} \frac{\mathrm{d}\boldsymbol{v}_{\mathrm{g}}}{\mathrm{d}t} = -\nabla P + \rho_{\mathrm{g}} \boldsymbol{f} + \sum_i K_i (\boldsymbol{v}_{\mathrm{d}_i} - \boldsymbol{v}_{\mathrm{g}}), \tag{3}$$

$$\rho_{\mathrm{d}_i} \frac{\mathrm{d}\boldsymbol{v}_{\mathrm{d}_i}}{\mathrm{d}t} = \rho_{\mathrm{d}_i} \boldsymbol{f} - K_i (\boldsymbol{v}_{\mathrm{d}_i} - \boldsymbol{v}_{\mathrm{g}}), \tag{4}$$

where P is the gas pressure, $\boldsymbol{f}$ is any body forces acting on the fluids, typically gravity from a star or planet (we ignore self-gravity in this paper), and K_i is the drag coefficient between the gas and a particular dust species, i. Note that each dust fluid has one gas drag interaction term, whereas the gas momentum equation has a sum of interactions over each dust species. Also, note that the dust has no pressure gradient force term. In general, the drag coefficient could be a complicated expression. We assume that the drag force is linear with respect to the differential velocity, $\Delta \boldsymbol{v}_i = \boldsymbol{v}_{\mathrm{d}_i} - \boldsymbol{v}_{\mathrm{g}}$. Thus, the drag coefficient is constant in differential velocity.

The gas and dust exchange momentum via drag which leads to frictional heating. Under the assumption that the gas and dust grains are at the same temperature, the evolution of gas internal energy is given by

$$\rho_{\mathrm{g}} \frac{\mathrm{d}u_{\mathrm{g}}}{\mathrm{d}t} = -P(\nabla \cdot \boldsymbol{v}_{\mathrm{g}}) + \rho_{\mathrm{g}} \sum_i K_i (\boldsymbol{v}_{\mathrm{g}} - \boldsymbol{v}_{\mathrm{d}_i})^2. \tag{5}$$

We neglect the dust fluid internal energy under the assumption that the dust and gas are at the same temperature.

Equations (1)–(5) are $2N + 3$ equations describing the evolution of a mixture of gas and N dust species. We discretize these equations with SPH in Section 2.3.

2.2 Drag time-scale

2.2.1 *Drag coefficient and stopping time*

Dust and gas interact via a drag force. This drag force has a characteristic time-scale, known as the stopping time. The stopping time relates to the drag coefficient, which depends on quantities such as the gas temperature and density, and on the physical characteristics of the dust grains. For a single dust species, the stopping time, t_{s}, is given by

$$t_{\mathrm{s}} = \frac{\rho_{\mathrm{g}} \rho_{\mathrm{d}}}{K(\rho_{\mathrm{g}} + \rho_{\mathrm{d}})}, \tag{6}$$

where K is the drag coefficient for the single species. We assume spherical grains of size s with a uniform material density, ϱ_{m}. In the linear Epstein regime (Epstein 1924), the drag coefficient K is

$$K = \frac{\rho_{\mathrm{g}} \rho_{\mathrm{d}}}{\varrho_{\mathrm{m}} s} \sqrt{\frac{8}{\pi \gamma}} c_{\mathrm{s}} f, \tag{7}$$

where γ is the adiabatic index of the gas. For convenience, we define an effective material density, ϱ_{eff}, given by $\varrho_{\mathrm{eff}} = \varrho_{\mathrm{m}} \sqrt{\pi \gamma / 8}$. In addition, f is a correction for supersonic relative velocities given by (Kwok 1975)

$$f = \sqrt{1 + \frac{9\pi}{128} \frac{\Delta v^2}{c_{\mathrm{s}}^2}}. \tag{8}$$

As discussed in Hutchison et al. (2018), a straightforward generalization of the stopping time for multiple dust species is not available. Each dust species is separately coupled to the gas by the drag force. However, the dust species are indirectly coupled to each other via backreaction, as required by conservation of momentum. Considering the multiple dust species case, and ignoring the supersonic correction factor, the drag coefficient, K_i, is now

$$K_i = \frac{\rho_{\mathrm{g}} \rho_{\mathrm{d}_i} c_{\mathrm{s}}}{\varrho_{\mathrm{eff}} s_i}. \tag{9}$$

By analogy with equation (6) we can define a 'stopping time', t'_{s_i}, as

$$t'_{\mathrm{s}_i} = \frac{\rho_{\mathrm{g}} \rho_{\mathrm{d}_i}}{K_i(\rho_{\mathrm{g}} + \rho_{\mathrm{d}_i})}. \tag{10}$$

However, there are other 'stopping times' we can define. First, we define $\rho = \rho_{\mathrm{g}} + \sum_i \rho_{\mathrm{d}_i}$ as the total density of the gas and all dust

species. Then, we can define another 'stopping time', t_{s_i}, as

$$t_{s_i} = \frac{\rho_g \rho_{d_i}}{K_i \rho}. \tag{11}$$

Considering the mixture of dust and gas as a whole, we define the weighted sum $s_{eff} = \sum_i \rho_{d_i} s_i / \sum_i \rho_{d_i}$ as an effective grain size for the mixture. Then, we can define an effective stopping time for the dust mixture, assuming Epstein drag, as

$$T_s = \frac{\varrho_{eff} s_{eff}}{\rho c_s}. \tag{12}$$

By combining equations (6) and (7), we can see the expression for the multigrain effective stopping time, T_s, is analogous to the single dust species case, t_s.

2.2.2 Stokes number

The Stokes number, St, is a dimensionless stopping time defined as the stopping time in units of a typical flow time. For protoplanetary discs, the typical flow time is the Keplerian orbital time, $1/\Omega_K$, so that the Stokes number is $St \equiv t_s \Omega_K$. Note that the Stokes number depends on the gas disc properties, via the density and temperature, the dust disc density, the dust grain properties, i.e. size and material density, and the stellar mass and orbital distance. The disc surface density, Σ, and disc scale height, H, are related to the density, sound speed, and Keplerian orbital time by $\rho = \Sigma/\sqrt{2\pi}H$ and $\Omega_K = c_s/H$. Using these relations, we can show that the Stokes number in the mid-plane of a protoplanetary disc is given by

$$St = \frac{\sqrt{2\pi}\varrho_{eff} s}{\Sigma}. \tag{13}$$

Considering the multiple dust species case, we can define an effective mid-plane Stokes number for the mixture using the effective stopping time (equation 12) as $St_{eff} = \sqrt{2\pi}\varrho_{eff} s_{eff}/\Sigma$. An alternative is to define a per species mid-plane Stokes number in analogy with the single grain size case:

$$St_i = \frac{\sqrt{2\pi}\varrho_{eff} s_i}{\Sigma_g \left(1 + \sum_i \varepsilon_i\right)}, \tag{14}$$

where Σ_g is the gas surface density and $\varepsilon_i = \rho_{d_i}/\rho_g$ is the dust-to-gas ratio for each dust species. Again, we see the combination of grain properties, size and material density, and the disc surface density fixing the Stokes number. Given that we assume the material density is the same for all species, we see that the grain size of the species, for any fixed location in the disc, gives the variation in Stokes number between species.

The Stokes number controls the dynamics of dust grains in protoplanetary discs (Weidenschilling 1977; Takeuchi & Lin 2002), affecting radial drift, vertical settling, orbital circularization, and gap and spiral formation. The individual Stokes number (equation 14) encapsulates the dynamics of each dust species. We can distinguish between three regimes of dust dynamics:

(i) small grains, i.e. those with $St_i \ll 1$,
(ii) intermediate-sized grains, i.e. those with $St_i \sim 1$, and
(iii) large grains, i.e. those with $St_i \gg 1$.

Small grains have short stopping time, i.e. differential velocity decays faster than the orbital time, and are thus strongly coupled to the gas. These grains stick to the gas, e.g. following the gas accretion flow. Large grains have long stopping time, i.e. differential velocity decays more slowly than the orbital time, and are thus weakly coupled to the gas. Intermediate-sized grains are marginally coupled to the gas. These grains experience the fastest radial drift velocities (Takeuchi & Lin 2002; Ayliffe et al. 2012). For a typical protoplanetary disc, with surface density $\approx$1 g cm^{-2} and intrinsic grain density $\approx$1 g cm^{-3}, small grains are $\lesssim$10 μm, and large grains are $\gtrsim$1 mm. Note that for other physical systems the terms small and large grains have different meaning. For example, in the interstellar medium large grains might be any grains $>$10 μm.

Several works describe the behaviour of these dust species as independently coupled to the gas (Nakagawa, Sekiya & Hayashi 1986; Dipierro & Laibe 2017; Kanagawa et al. 2017). Dipierro et al. (2018) extended the analysis to consider the full backreaction of all species on to the gas. They showed that the cumulative backreaction from multiple dust species can strongly affect the gas flow, even for low dust-to-gas ratio, and that, for large dust-to-gas ratio, the small grains can drift outwards, as opposed to the typical inwards drift. This gives motivation to this work.

2.3 SPH with multiple dust species

2.3.1 SPH density with multiple dust species

We extend the SPH method for dust and gas mixtures with a single species, first described in Monaghan & Kocharyan (1995) and improved upon by Laibe & Price (2012a,b), to multiple dust species. We use a separate set of particles to represent the gas and each dust species. So, each phase of the mixture has its own density and smoothing length that depend only on the neighbouring particles of its own phase. This differs from the 1-fluid method described by Hutchison et al. (2018) in which there is a single set of SPH particles representing the mixture. The SPH formulation of the continuity equations, equations (1)–(2), are given by

$$\rho_a^k = \sum_b m_b^k W_{ab}\left(h_b^k\right), \tag{15}$$

$$h_a^k = \eta \left(\frac{m_a^k}{\rho_a^k}\right)^{1/\nu}, \tag{16}$$

where the superscript $k \in \{g, d_1, \ldots, d_N\}$ is an index distinguishing between the gas and all dust species; ν is the number of spatial dimensions; m_a^k, ρ_a^k, and h_a^k are the SPH particle mass, density, and smoothing length, respectively; W_{ab} is the SPH smoothing kernel; and η is a factor of order unity which determines the number of neighbours per particle. For an overview on the SPH method, see Monaghan (1992, 2005) and Price (2012). So, there are $N + 1$ sets of equations, equations (15)–(16), one set per phase. This is a straightforward generalization of previous single dust species methods.

One important feature of the above equations is that the gas and dust densities (for each dust species) are calculated without reference to any other phase. Given that the dust is pressureless, this can lead to dust becoming trapped under the gas resolution (Laibe & Price 2012a). This is in contrast to the gas in which, due to the pressure force, particles are kept apart to prevent this overconcentration. Dust and gas interact only via drag which requires relative motion. If dust particles become concentrated and remain motionless with respect to the local gas distribution there is no pressure force to stop further collapse. This can lead to unphysical clumping of dust which can mimic physical clumping of dust that might be expected, in, for example, protoplanetary discs or molecular clouds. (See Tricco, Price & Laibe 2017, for a discussion of this in the context of molecular clouds.)

2.3.2 SPH equation of motion with multiple dust species

The equations of motion in SPH can be derived from a Lagrangian giving exact conservation of linear and angular momentum, and energy (Price 2012). Following Laibe & Price (2012a) and Price & Laibe (2020), the equation of motion for the gas is given by

$$\frac{\mathrm{d}\boldsymbol{v}_a^{\mathrm{g}}}{\mathrm{d}t} = -\sum_{b\in g} m_b^{\mathrm{g}} \left[\frac{P_a + q_{ab}^a}{\Omega_a^{\mathrm{g}} \left(\rho_a^{\mathrm{g}}\right)^2} \nabla_a W_{ab}\left(h_a^{\mathrm{g}}\right) + \frac{P_b + q_{ab}^b}{\Omega_b^{\mathrm{g}} \left(\rho_b^{\mathrm{g}}\right)^2} \nabla_a W_{ab}\left(h_b^{\mathrm{g}}\right) \right] + \nu \sum_{i=1}^{N} \sum_{b\in d_i} m_b^{\mathrm{g}} \frac{K_{ab}}{\rho_a^{\mathrm{g}} \rho_b^{\mathrm{d}_i}} (\boldsymbol{v}_{ab}^* \cdot \hat{\boldsymbol{r}}_{ab}) \hat{\boldsymbol{r}}_{ab} D_{ab}(h_{\max}), \tag{17}$$

where K_{ab}, D_{ab}, $h_{\max}$, and $\boldsymbol{v}_{ab}^*$ are defined below. P_a refers to the pressure on particle a, Ω_a^{g} is a term related to the variable smoothing length given by

$$\Omega_a^{\mathrm{g}} = 1 - \frac{\partial h_a}{\partial \rho_a} \sum_b m_b \frac{\partial W_{ab}(h_a)}{\partial h_a}. \tag{18}$$

q_{ab}^a and q_{ab}^b are terms relating to artificial viscosity given by

$$q_{ab}^a = \begin{cases} -\frac{1}{2}\rho_a v_{\mathrm{sig},a} \boldsymbol{v}_{ab} \cdot \hat{\boldsymbol{r}}_{ab}, & \boldsymbol{v}_{ab} \cdot \hat{\boldsymbol{r}}_{ab} < 0, \\ 0, & \text{otherwise}, \end{cases} \tag{19}$$

where $\hat{\boldsymbol{r}}_{ab} = (\boldsymbol{r}_a - \boldsymbol{r}_b)/|\boldsymbol{r}_a - \boldsymbol{r}_b|$ is the normalized separation vector, $\boldsymbol{v}_{ab} = \boldsymbol{v}_a - \boldsymbol{v}_b$, and $v_{\mathrm{sig},a}$ is the maximum signal speed given by

$$v_{\mathrm{sig},a} = \alpha_a^{\mathrm{AV}} c_{s,a} + \beta^{\mathrm{AV}} |\boldsymbol{v}_{ab} \cdot \hat{\boldsymbol{r}}_{ab}|, \tag{20}$$

where α_a^{AV} and β^{AV} are parameters controlling the artificial viscosity strength. The first term in equation (17) represents the usual SPH discretization of the pressure gradient force on a particle, labelled by a. The sum, denoted by $\sum_{b\in g}$, is a sum over gas neighbours, labelled by b. The second term is discussed in Section 2.3.3.

The equation of motion for each dust species, d_i, is given by

$$\frac{\mathrm{d}\boldsymbol{v}_a^{\mathrm{d}_i}}{\mathrm{d}t} = -\nu \sum_{b\in g} m_b^{\mathrm{d}_i} \frac{K_{ab}}{\rho_b^{\mathrm{g}} \rho_a^{\mathrm{d}_i}} (\boldsymbol{v}_{ab}^* \cdot \hat{\boldsymbol{r}}_{ab}) \hat{\boldsymbol{r}}_{ab} D_{ab}(h_{\max}), \tag{21}$$

where K_{ab} is the drag coefficient between particles a and b, D_{ab} is the drag kernel (Section 2.3.3), $h_{\max} = \max(h_a, h_b)$ is the maximum smoothing length between any pair of particles, and $\boldsymbol{v}_{ab}^*$ refers to a higher order reconstructed velocity for the particle pair a and b (Price & Laibe 2020). This avoids the 'overdamping' problem described by Laibe & Price (2012a).

2.3.3 Drag kernel and drag coefficient

The second term in equation (17) represents the cumulative drag force from each dust species on particle a (with $i \in \{1, \ldots, N\}$ representing each species). For each species, the sum, denoted by $\sum_{b\in d_i}$, is a sum over dust neighbours, labelled by b, where here the a index refers to the gas particle and the b index refers to its dust neighbours. Similarly, the sum on the right-hand side of equation (21) represents the drag force from the gas on the particular dust species, where a refers to a dust (SPH) particle and b refers to its gas neighbours.

Equations (17) and (21) are a straightforward generalization of Laibe & Price (2012a) to multiple dust species. For Epstein drag, the drag coefficient K_{ab} is given by

$$K_{ab} = \frac{\rho_a^{\mathrm{g}} \rho_b^{\mathrm{d}_i}}{\varrho_{\mathrm{eff}} s_i} c_{s,a} f_{ab}, \tag{22}$$

where $c_{s,a}$ is the sound speed on the gas particle and f_{ab} supersonic correction factor (equation 8) between the two particles.

The typical bell-shaped kernel used in SPH to estimate density, denoted by W_{ab}, is not appropriate for the drag force summation. Rather, we use a separate drag kernel, D_{ab}, with a 'double-hump'. This was found to be 10× more accurate (Laibe & Price 2012a).

2.4 Time-stepping

2.4.1 Time-step constraint

We use an explicit leapfrog time-stepping scheme as discussed in Price et al. (2018a). Given that we use an explicit scheme for the drag term there is an additional stability constraint on the time-step Δt. We derive this constraint for the forward Euler scheme. (Even though we do not use this scheme, it provides a guide to the nature of the constraint.) Following Laibe & Price (2012a, 2014c), we start with the discretization of the drag-only velocity equations for dust and gas with the forward Euler method, we have

$$\frac{v_{\mathrm{g}}^{n+1} - v_{\mathrm{g}}^n}{\Delta t} = -\sum_i \frac{K_i}{\rho_{\mathrm{g}}} \left(v_{\mathrm{g}}^n - v_{\mathrm{d}_i}^n\right), \tag{23}$$

$$\frac{v_{\mathrm{d}_i}^{n+1} - v_{\mathrm{d}_i}^n}{\Delta t} = \frac{K_i}{\rho_{\mathrm{d}_i}} \left(v_{\mathrm{g}}^n - v_{\mathrm{d}_i}^n\right). \tag{24}$$

Then we perform a von Neumann stability analysis, where we expand the solution in plane waves, $v_j^m = V_j^m e^{ikx}$, where j refers to the species, k is the wavenumber, and m refers to the time-step. This expansion leads to the following matrix equation:

$$\begin{pmatrix} V_{\mathrm{g}} \\ V_{d_1} \\ \vdots \\ V_{d_N} \end{pmatrix}^{n+1} = \begin{pmatrix} 1 - \frac{\Delta t \sum K_i}{\rho_{\mathrm{g}}} & \frac{\Delta t K_1}{\rho_{\mathrm{g}}} & \cdots & \frac{\Delta t K_N}{\rho_{\mathrm{g}}} \\ \frac{\Delta t K_1}{\rho_{d_1}} & 1 - \frac{\Delta t K_1}{\rho_{d_1}} & \cdots & 0 \\ \vdots & \vdots & \vdots & \vdots \\ \frac{\Delta t K_N}{\rho_{d_N}} & 0 & \cdots & 1 - \frac{\Delta t K_N}{\rho_{d_N}} \end{pmatrix} \times \begin{pmatrix} V_{\mathrm{g}} \\ V_{d_1} \\ \vdots \\ V_{d_N} \end{pmatrix}^n. \tag{25}$$

To find the eigenvalues of the matrix M above we need to find the characteristic polynomial, $\det(M - \lambda I)$. We can find the determinant of M using Schur's determinant identity $\det(M) = \det(A - BD^{-1}C)\det(D)$, where A is the 1×1 matrix consisting of the upper left value, B is the $N \times 1$ matrix of the top row except the first value, C is the $1 \times N$ matrix of the left-hand column except the first value, and D is the remaining $N \times N$ diagonal matrix. Applying this identity to the matrix $M - \lambda I$ gives

$$\left(1 - \frac{\Delta t \sum K_i}{\rho_{\mathrm{g}}} - f - \lambda\right) \times \prod_i \left(1 - \frac{\Delta t K_i}{\rho_{\mathrm{d}_i}} - \lambda\right), \tag{26}$$

where $f = \sum_i \Delta t^2 K_i^2 [\rho_{\mathrm{g}} \rho_{\mathrm{d}_i} (1 - \frac{\Delta t K_i}{\rho_{\mathrm{d}_i}} - \lambda)]^{-1}$. We neglect f as it is second order in Δt. To find the eigenvalues we equate the characteristic polynomial with zero and solve to find

$$\lambda_{\mathrm{g}} = 1 - \frac{\Delta t \sum_i K_i}{\rho_{\mathrm{g}}} \quad \text{and} \quad \lambda_{\mathrm{d}_i} = 1 - \frac{\Delta t K_i}{\rho_{\mathrm{d}_i}}. \tag{27}$$

For stability, we require $|\lambda_k| < 1$. Using this condition with equations (9) and (11) gives the following time-step criteria:

$$\Delta t < \frac{2}{\sum_i \epsilon_i / t_{s_i}} \quad \text{and} \quad \Delta t < \frac{2 t_{s_i}}{1 - \epsilon} \quad \forall\, i, \tag{28}$$

where $\epsilon = \sum_i \epsilon_i$ and $\epsilon_i = \rho_{\mathrm{d}_i}/\rho$. We have $N + 1$ inequalities. We take the minimum over dust stopping times in the inequality on the

right to find the most restrictive time-step criterion involving only dust quantities:

$$\Delta t < \frac{2}{1-\epsilon} \min_i t_{s_i}. \tag{29}$$

Laibe & Price (2014c) derived more general bounds on the eigenvalues of the drag matrix that imply a time-step criterion:

$$\Delta t < \left(\max_i \left(\frac{1}{\epsilon_i t'_{s_i}} \right) + \frac{1}{1-\epsilon} \sum_i t'_{s_i} \right)^{-1}. \tag{30}$$

Assuming strong drag, this can be approximated by

$$\Delta t < \left(\frac{1}{\min_i t_{s_i}} + \frac{1}{(1-\epsilon) t'_{s_i}} \right)^{-1}. \tag{31}$$

We take the minimum over dust stopping times in the first term of the inequality to find the most restrictive time-step criterion given by

$$\Delta t < \frac{2}{N} \frac{\max_i t_{s_i}}{\min_i \epsilon_i}. \tag{32}$$

This is a sufficient but not necessary condition. Given that N is of order tens and, at worst, $\min_i \epsilon_i \sim 1$, we can say that equation (29) is more restrictive than equation (32), and thus provides the time-step constraint for drag. Note that (i) the stability constraint depends on the shortest stopping time, and (ii) for large dust-to-gas ratios, i.e. $\epsilon \to 1$, the stability constraint becomes unimportant.

This time-step constraint is not the same as the one derived in Laibe & Price (2012a) for a single dust species. In that case, the time-step constraint is the stopping time itself, and does not depend on the dust fraction. Note that we have shown that equation (29) is the stability constraint for the forward Euler discretization of the drag terms to first order in Δt. We have not derived the stability constraint for the leapfrog scheme we use in our numerical tests below, but we expect the stability constraint to remain the same.

2.4.2 *Time-step constraint for SPH*

We can rewrite the time-step constraint in equation (29) using the alternative stopping time, t'_{s_i} (defined in equation 10). First, we note that $t_{s_i}/(1-\epsilon) = \rho_{d_i}/K_i$ and $t'_{s_i}(1+\varepsilon_i) = \rho_{d_i}/K_i$. Then, given that $1-\epsilon$ does not depend upon the index i, we can bring it under the min operator to give

$$\Delta t < 2 \min_i \{ t'_{s_i} (1+\varepsilon_i) \}. \tag{33}$$

This is useful because in evolving the momentum equations we use the drag coefficient on a dust (or gas) particle over its gas (or dust) neighbours, without reference to the other dust species. Given that $\varepsilon_i > 0$, for simplicity, we take the more restrictive constraint of setting $\varepsilon_i = 0$, i.e.

$$\Delta t < 2 \min_i t'_{s_i}. \tag{34}$$

Even though using a factor of 2 in equation (34) provides a numerically stable time-stepping scheme (in the von Neumann sense), numerical experimentation showed that any value greater than 1.0 led to inaccurate results. We use $C_{\rm drag}$ to refer to this factor.

For a dust particle, we take the minimum over gas neighbours (labelled by a) of the individual species constraint ($\Delta t < C_{\rm drag} t_{s_i}$):

$$\Delta t < C_{\rm drag} \min_a \left\{ \frac{\rho_a^{\rm g} \rho_b^{{\rm d}_i}}{K_{ab} \left(\rho_a^{\rm g} + \rho_b^{{\rm d}_i} \right)} \right\}, \tag{35}$$

whereas, for a gas particle, we take the minimum of equation (34), rewritten in terms of the drag coefficient and densities, over the neighbouring dust particles (labelled by b) to find the SPH time-step constraint for a particle:

$$\Delta t < C_{\rm drag} \min_i \min_b \left\{ \frac{\rho_a^{\rm g} \rho_b^{{\rm d}_i}}{K_{ab} \left(\rho_a^{\rm g} + \rho_b^{{\rm d}_i} \right)} \right\}. \tag{36}$$

3 NUMERICAL TESTS

We implemented the numerical method described in Section 2.3 in the SPH code PHANTOM.[1] We then performed several tests to validate the method against known analytical solutions. The dusty box test (Section 3.1) validates the drag force coupling in the absence of spatial gradients. The dusty wave test (Section 3.2) validates the method with spatial gradients in a linear regime. The dusty shock test (Section 3.3) validates the method in a challenging non-linear regime. The radial drift test (Section 3.4) validates the method is the context of a global 3D protoplanetary disc model.

The tests all have analytical solutions in one spatial dimension. We performed each of the tests in three dimensions, and then reduced the data to one dimension for comparison with the analytical solutions. In each of the tests we used, unless stated otherwise: a globally isothermal equation of state; the quintic kernel with 113 mean particle neighbours ($\eta = 1.0$ in equation (15)); global time-stepping, i.e. all particles have the same time-step; a Courant factor of 0.3; a time-step constraint on the acceleration $C_{\rm force}$ of 0.25, where $\Delta t_a < C_{\rm force} \sqrt{h_a/|\boldsymbol{a}_a|}$; and a time-step constraint on the drag $C_{\rm drag}$ of 0.9.

3.1 Dusty box

We performed the multigrain version of the dusty box test described in Laibe & Price (2011). We set up a periodic box of uniform density gas and dust with an initial differential velocity between the gas and each dust species. In this test, the equation of motion simplifies to

$$\frac{\partial \Delta \boldsymbol{V}}{\partial t} = -\Omega \Delta \boldsymbol{V}, \tag{37}$$

where $\Delta \boldsymbol{V}$ is the differential velocity vector in the direction of motion, i.e. $\boldsymbol{v}_{{\rm d}_i} - \boldsymbol{v}_{\rm g}$ for each i projected along the direction of motion, and Ω is the drag matrix (equation 65 of Laibe & Price 2014c) given by

$$\Omega_{ij} = \begin{cases} \frac{1}{t''_{s_i}} \frac{1}{(1-\varepsilon)}, & i \neq j, \\ \frac{1}{t''_{s_i}} \left(\frac{1}{\varepsilon_i} + \frac{1}{1-\varepsilon} \right), & i = j, \end{cases} \tag{38}$$

where $\varepsilon = \sum_i \varepsilon_i$, and $t''_{s_i} = (\sum_i \rho_i)/K_i$.

This problem tests how well the numerical scheme captures the exchange of momentum between gas and each dust species via the drag force. All tests were in the linear Epstein drag regime. We performed six tests in two sets of three. The first set had a total dust-to-gas ratio of 0.01, and the second set 0.5. The tests within each set had 1, 2, and 5 dust species, respectively, with grain sizes given in Table 1. Each test had equal mass in each grain size bin. The gas is initially motionless, and each dust species has uniform velocity in the positive x-direction. We turned off the SPH viscosity, i.e. set $\alpha_{\rm AV}$ to zero in PHANTOM. We set $C_{\rm drag} = 0.2$ for computational reasons (to allow PHANTOM to output data more frequently while still restricting the time-step via the drag force).

[1] See the git commit labelled by the hash `64dbd2b1` in the PHANTOM source code repository for the implemented changes.

Table 1. Grain sizes for dusty box test.

Species	Grain size (cm)
One dust species	
1	0.01
Two dust species	
1	0.01
2	0.1
Five dust species	
1	0.01
2	0.0316
3	0.1
4	0.316
5	1.0

For each test problem, we set up each of the gas and dust fluids on a close-packed lattice, using dense-sphere packing, such that there were 648 particles per species (eight particles in the direction of motion). We set the gas density to 10^{-13} g cm^{-3}, with the dust-to-gas ratio varying per test problem. We set the dust grain material density for all species to 1.0 g cm^{-3}.

Fig. 1 shows the time evolution of the mean velocity differential between the gas and each dust species, compared with analytical solutions. The time is a dimensionless time-scaled by the stopping time, t_{s_i}, of the smallest grain size, which is 9.677, 19.354, and 48.385 yr for the low dust-to-gas ratio (0.01) calculations (top row), and 0.287, 0.575, and 1.437 yr for the high dust-to-gas ratio (0.5) calculations (bottom row). Given that there are no spatial gradients in the problem, all particles follow the mean velocity. The dashed lines represent the analytical solution without backreaction from the dust on the gas. The solid lines represent the analytical solution including backreaction.

For low dust-to-gas ratio (0.01) both analytical solutions give the same decay of differential velocity, with which the PHANTOM simulation agrees. For a larger dust-to-gas ratio (0.5) the analytical solutions for multiple species differs from the single-species solution, and the PHANTOM simulation data follows the backreaction-inclusive solution. In all cases, the numerical solution matches the analytical solution with relative error less than 0.01.

Fig. 2 shows a zoomed version of the bottom right-hand panel in Fig. 1. For large dust-to-gas ratio we see that the smallest grains (0.01 cm) rapidly slow and the differential velocity reverses sign. That is the small grains slow to the gas velocity; then, as the larger grains speed up the gas via drag, the gas drags the small grains along with it. This shows that the behaviour of multiple dust species for large dust-to-gas ratios requires taking backreaction into consideration to capture the physics of dust drag accurately (Gonzalez, Laibe & Maddison 2017; Dipierro et al. 2018).

Fig. 3 shows that the method is second-order accurate with respect to the time-step. Each marker represents the L2-norm error, of a numerical solution for the two dust species case with a dust-to-gas ratio of either 0.01 or 0.5, with varying time-step controlled by $C_{\rm drag}$. The error is given by

$$\text{error}(\Delta t) = \sqrt{\sum_{i,j} \left(V_{i,j}^{\Delta t} - v_j(t_i)\right)^2}, \tag{39}$$

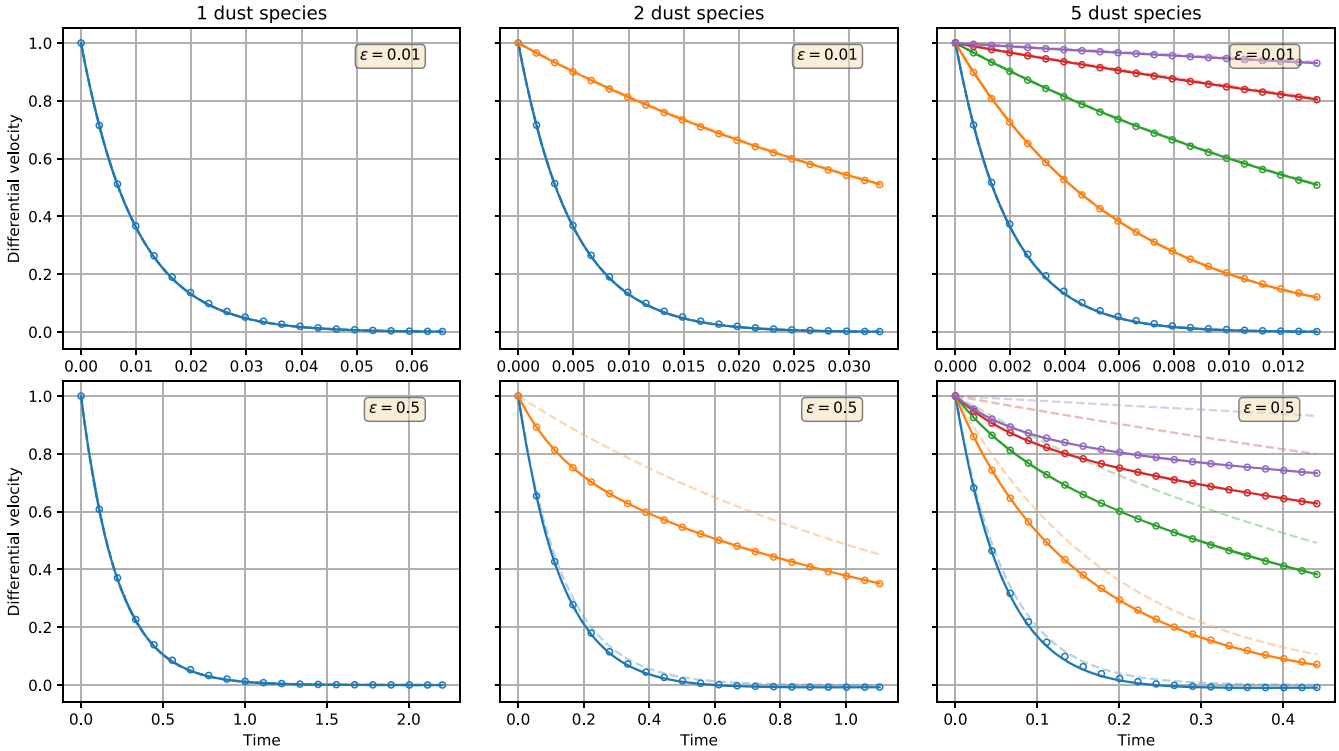

Figure 1. Dusty box numerical test showing the differential velocity between the dust and gas. The total dust-to-gas ratio is 0.01 (top row) and 0.5 (bottom row). From left to right: the number of dust species is 1, 2, 5. The open circles represent the results from the PHANTOM numerical solution. The solid and dashed lines represent the analytical solution with and without taking backreaction into account, respectively. In the top row, the solid and dashed lines lie on top of each other. In the bottom row, the numerical solution matches the analytical solution including backreaction. Each colour represents the differential velocity of a dust species increasing in size from bottom to top. For the specific grain sizes, see Table 1. Time is dimensionless, scaled by the shortest stopping time.

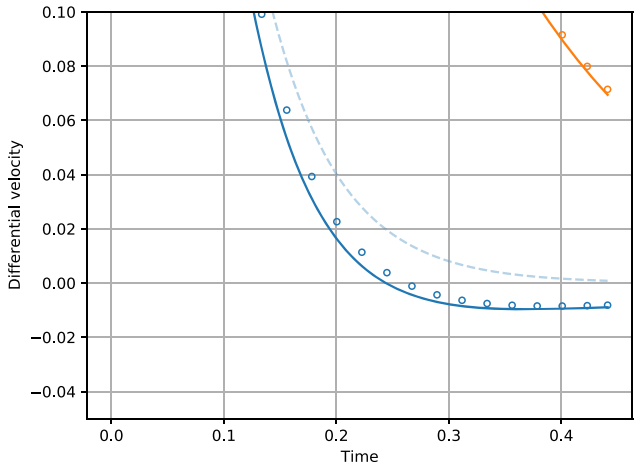

Figure 2. Zoomed-in version of bottom right-hand panel in Fig. 1. The smallest dust grains (in blue) show a negative differential velocity.

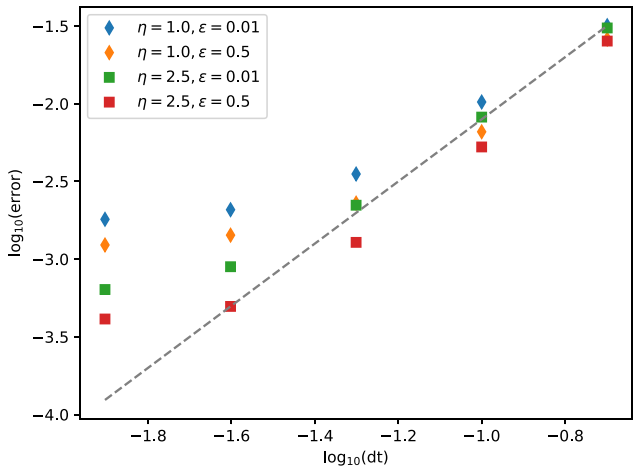

Figure 3. The L2-norm error with varying time-step showing the second-order convergence of the method. Each marker represents a single simulation with two dust species with a dust-to-gas ratio of either 0.01 or 0.5. The grey-dashed line represents a slope of 2. For large time-steps, the error matches the line of slope 2 (indicating second-order convergence). For smaller time-steps the error is dominated by kernel bias. The diamond and the square markers represent numerical solutions with $\eta = 1.0$ and $\eta = 2.5$, respectively.

where the indices i and j represent time and dust species, respectively, $V_{i,j}^{\Delta t}$ is the numerical solution for a particular Δt (or equivalently $C_{\rm drag}$), and $v_j(t_i)$ represents the exact solution. For large time-steps, the error matches the grey, dashed line of slope 2 (indicating second-order convergence in the log–log plot). For smaller time-steps the error is dominated by kernel bias. This is demonstrated by the fact that in the case with fewer neighbours ($\eta = 1.0$), indicated by diamond markers, the error plateaus at a larger magnitude than for the case with a greater number of neighbours ($\eta = 2.5$), indicated by the square markers.

3.2 Dusty wave

We performed the multigrain version of the dusty wave test described in Laibe & Price (2011, 2014c). This is a test of the dust–gas drag coupling in the context of a damped sound wave. The dust is a pressureless fluid and cannot support sound waves. However, the gas can support sounds waves and drags the dust. This leads to damping of the wave. This tests the numerical method in a problem including spatial gradients in a linear regime.

Table 2. Mean density and stopping times for dusty wave test.

Species	Density	Stopping time
One dust species		
g	1.0	–
1	2.24	0.4
Four dust species		
g	1.0	–
1	0.1	0.1
2	0.2333	0.2154
3	0.3667	0.4642
4	0.5	1.0

Considering small perturbations around an equilibrium state, $\rho_j = \rho_j^0 + \delta\rho_j$, and $v_j = \delta v_j$, where the index j is g for the gas species, and d_i for each of the dust species, the linearised equations of motion for this system are

$$\frac{\partial \delta\rho_{\rm g}}{\partial t} + \rho_{\rm g}^0 \frac{\partial \delta v_{\rm g}}{\partial x} = 0, \tag{40}$$

$$\frac{\partial \delta\rho_{\rm d_i}}{\partial t} + \rho_{\rm d_i}^0 \frac{\partial \delta v_{\rm d_i}}{\partial x} = 0, \tag{41}$$

$$\rho_{\rm g}^0 \frac{\partial \delta v_{\rm g}}{\partial t} = \sum_i K_i(\delta v_{\rm d_i} - \delta v_{\rm g}) + c_s^2 \frac{\partial \delta\rho_{\rm g}}{\partial x}, \tag{42}$$

$$\rho_{\rm d_i}^0 \frac{\partial \delta v_{\rm d_i}}{\partial t} = -K_i(\delta v_{\rm d_i} - \delta v_{\rm g}). \tag{43}$$

For the particular set-up, we followed Benítez-Llambay et al. (2019). By assuming solutions to the linearised equations of the form $\delta f = \delta\hat{f} e^{ikx - i\omega t}$ they derive solutions as a dispersion relation (their equation 45) and associated set of eigenfunctions (their equations 46–48). Following Benítez-Llambay et al. (2019), we set the initial condition to constant density and zero velocity plus a perturbation of the form

$$\delta f = A[\mathrm{Re}(\delta\hat{f})\cos(kx) - \mathrm{Im}(\delta\hat{f})\sin(kx)]. \tag{44}$$

We set the sound speed $c_{\rm s} = 1$, and the wave amplitude A to $10^{-4}c_{\rm s}$ and $10^{-4}\rho_{\rm g}^0$ for the velocity and density perturbations, respectively.

We performed two tests: (1) with gas and a single dust species, and (2) with gas and four dust species. We set the background density, drag coefficients, and initial perturbations from table 2 in Benítez-Llambay et al. (2019). We set up a periodic box of unit length, with 8192 particles for each species (128 particles in the wave direction). We use constant drag, K_i, for each dust species, where $K_i = \rho_{\rm d_i}/t_{s_i}$, and $\rho_{\rm d_i}$ and t_{s_i} from Table 2 (following Benítez-Llambay et al. 2019). We turned off the SPH viscosity, i.e. set $\alpha_{\rm AV}$ to zero in PHANTOM.

Fig. 4 shows the time evolution of the normalized velocity and density perturbations at a particular location within the domain ($x = 0$). The normalized velocity v_N and density ρ_N are defined by

$$\rho_N = \frac{\overline{\rho} - \overline{\rho}_0}{A\overline{\rho}_0}, \tag{45}$$

$$v_N = \frac{\overline{v}}{Ac_s}, \tag{46}$$

where the zero subscript represents the initial value. The solid lines represent the analytical solution from Benítez-Llambay et al. (2019) and the open circles represent the numerical solution from PHANTOM. We see that the numerical solution accurately reproduces the analytical solution, i.e. the relative error is everywhere less than

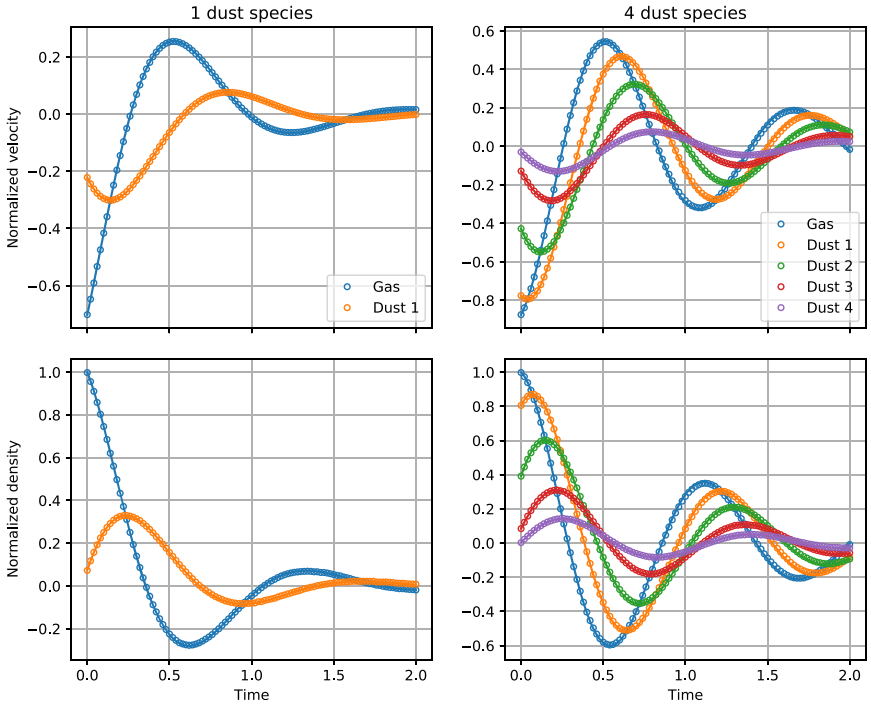

Figure 4. Dusty wave numerical test showing the normalized velocity (top) and density (bottom) perturbation at $x = 0$, for gas with one dust species (left) and gas with four dust species (right). The open circles represent the PHANTOM simulation, and the solid line represents the analytical solution from Benítez-Llambay et al. (2019). The gas is blue, and other colours represent different dust species.

0.01. In both cases, we see the wave damping effect, and within a few wave periods the wave dissipates.

3.3 Dusty shock

We performed a multiple species version of the isothermal steady state single species dusty shock test, with exact solution given in Lehmann & Wardle (2018).[2] Benítez-Llambay et al. (2019) generalized that solution to multiple dust species. The solution, in steady state, for this shock is described by the following set of equations:

$$\frac{\partial}{\partial x}(\rho_{\rm g} v_{\rm g}) = 0, \tag{47}$$

$$\frac{\partial}{\partial x}(\rho_{{\rm d}_i} v_{{\rm d}_i}) = 0, \tag{48}$$

$$\frac{\partial}{\partial x}\left[\rho_{\rm g}\left(v_{\rm g}^2 + c_s^2\right)\right] = -\sum_{i=1}^{N} K_i (v_{\rm g} - v_{{\rm d}_i}), \tag{49}$$

$$\frac{\partial}{\partial x}\left(\rho_{{\rm d}_i} v_{{\rm d}_i}^2\right) = K_i (v_{\rm g} - v_{{\rm d}_i}). \tag{50}$$

We assume a constant drag coefficient K_i per species. The constant isothermal sound speed is c_s. In steady state, due to the drag force, the gas and all dust species have the same pre-shock velocity $v_{\rm s}$ and the same asymptotic post-shock velocity. We define normalized velocities $\omega_{\rm g} = v_{\rm g}/v_{\rm s}$ and $\omega_{{\rm d}_i} = v_{{\rm d}_i}/v_s$, then these equations can be integrated to give

[2]The solution is described as a J-type shock in which the fluid variables undergo a jump discontinuity, rather than the properties being continuous across the front (as in a C-type shock).

Table 3. Dusty shock parameters. Same as Benítez-Llambay et al. (2019).

Fluids	K_1	K_2	K_3	ρ^-	ρ^+	ω^-	ω^+
2	1.0	–	–	1.0	8.0	1.0	0.125
4	1.0	3.0	5.0	1.0	16.0	1.0	0.0625

$$0 = \omega_{\rm g}^2 + \omega_{\rm g}\left[\sum_i \varepsilon_i(\omega_{{\rm d}_i} - 1) - \mathcal{M}^{-2} - 1\right] + \mathcal{M}^{-2}, \tag{51}$$

$$\frac{{\rm d}\omega_{{\rm d}_i}}{{\rm d}x} = \frac{K_i}{\rho_{{\rm d}_i}}(\omega_{\rm g} - \omega_{{\rm d}_i}), \tag{52}$$

where x_0 is the shock position and $\mathcal{M} = v_s/c_s$ is the Mach number (Benítez-Llambay et al. 2019). These equations can be numerically integrated to give the normalized velocities. Then, equations (47) and (48) give the densities:

$$\rho_j = \frac{\rho_j(x_0) v_j(x_0)}{v_j}, \tag{53}$$

where the index j refers to either g or ${\rm d}_i$.

We set up two tests. One test with a single dust species to validate against previous single dust species tests. And another test with three dust species to validate our multiple dust species method. We used that same parameters as shown in table 3 in Benítez-Llambay et al. (2019) reproduced here in Table 3 for completeness. For both tests, we chose $\mathcal{M} = 2$, $c_{\rm s} = 1$, and $\varepsilon_i = 1$ for all dust species. The left (pre-shock) velocities are set be the Mach number, i.e. $v_j = 2$, where j represents both gas and all dust species. We set the left (pre-shock) gas density $\rho_{\rm g}$ to 1. We set the drag coefficients K_i to: 1.0 for the single dust species test, and 1.0, 3.0, and 5.0 for the three dust species test. The right (post-shock) asymptotic values are given by

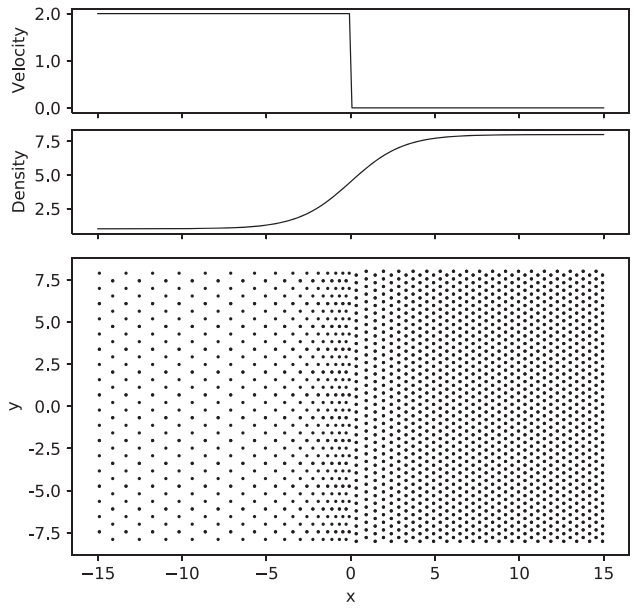

Figure 5. Dusty shock initial conditions. We used a step function for the velocity profile (top), and a smoothed density profile (middle). The particles for each species are placed on two close packed lattices, one on either side of the shock (bottom). The density is lower in the pre-shock region, on the left, than on the right. The particle positions in the shock region are adjusted to smooth the shock over a few particle spacings.

$$\rho_j^{\rm R} = \frac{\rho_j^{\rm L}\omega_j^{\rm L}}{\omega_j^{\rm R}}, \tag{54}$$

$$\omega_j^{\rm R} = (1+N)^{-1}\mathcal{M}^{-2}, \tag{55}$$

where j represents both gas and all dust species, N is the number of dust species, and the superscripts L and R represent left and right asymptotic states, respectively. We set $\alpha_{\rm AV}$ to 1.

We set up initial conditions such that the velocities are constant with their asymptotic values on either side of the shock at $x_{\rm shock} = 0$. We set up the densities similarly except that we smoothed the shock at shock boundary, using a logistic function, i.e.

$$\rho(x) = \frac{\rho_{\rm L}e^{-kx} + \rho_{\rm R}}{1+e^{-kx}}, \tag{56}$$

where $\rho_{\rm L}$ and $\rho_{\rm R}$ are the density on the left and right of the shock, respectively, and k is a factor determining the width of the smoothing. We set k^{-1} to $2x_{\rm sep}$, where $x_{\rm sep} = 0.1953125$ is the (resolution-dependent) separation between particles in the x-direction in the low-density region. This is due to the large (in principle, infinite) gradient in density at the shock boundary leading to an overconcentration of dust in the post-shock region.

Fig. 5 shows a sample of the initial particle positions (bottom) with the analytical density profile (top). For the gas and each dust species, we set up the particles on two close-packed lattices; one on each side of the shock, with the density and velocity set by their asymptotic values. We use the same resolution for the gas and each dust species. Due to the resolution following the mass in SPH, the numerical resolution is higher in the high-density region.

Fig. 6 shows the velocity and density of both tests at $t = 300$ which is long enough so that any transient behaviour has died out. We have binned the particles into 40 bins in the x-direction and calculated a mass-weighted average for both density and velocity. We have overplotted the analytical solution for comparison. Note that the shock position has drifted from its initial position, perhaps, due to numerical dissipation. We have shifted the analytical solution shock position to minimize the error, as in Benítez-Llambay et al. (2019). Note that this drift has velocity ∼0.5 per cent of the pre-shock velocity, and ∼5 per cent of the post-shock velocity. Our numerical method reproduces the exact solution in this non-linear test problem.

To achieve an accurate solution, we used a larger number of particle neighbours in the SPH density sum than is typical in dust–gas simulations with PHANTOM. The typical mean neighbour number when using the quintic kernel, used by default for dust–gas simulations, in calculating density sums is 113 (Price et al. 2018a). The mean neighbour number $\overline{N}_{\rm neigh}$ is related to the proportionality constant η by

$$\overline{N}_{\rm neigh} = \frac{4}{3}\pi(R_{\rm kern}\eta)^3. \tag{57}$$

For the quintic kernel, $R_{\rm kern} = 3.0$. So, by default, $\eta = 1.0$. We used a η value of 1.8 in Fig. 6.

Fig. 7 shows the comparison between the analytical and numerical solutions for the density varying the value of $\eta = 1.2, 1.5, 1.8$, corresponding to $\overline{N}_{\rm neigh} = 195, 381, 660$. We can see that the accuracy of the gas density (blue line and markers) is independent (or weakly dependent) on the neighbour number. In contrast, the dust density depends strongly on the neighbour number. To avoid large errors, we require $\eta = 1.5$, for the single dust species case, and $\eta = 1.8$, for the three dust species case. We discuss the implications of this in Section 4 below.

3.4 Radial drift

We tested the method against the steady-state radial drift solution for a viscous protoplanetary disc with multiple dust species calculated in Dipierro et al. (2018) as a generalization of the single species solution in Nakagawa et al. (1986) and the multiple species inviscid case in Bai & Stone (2010b). Following Dipierro et al. (2018), the gas radial drift velocity $v_{\rm R}^{\rm g}$ is given by

$$v_{\rm R}^{\rm g} = \frac{-\lambda_1 v_{\rm P} + (1+\lambda_0)\, v_{\rm visc}}{(1+\lambda_0)^2 + \lambda_1^2}, \tag{58}$$

and the dust radial drift velocity $v_{\rm R}^{\rm d_i}$ is given by

$$v_{\rm R}^{\rm d_i} = \frac{v_{\rm P}\left[(1+\lambda_0)\,{\rm St}_i - \lambda_1\right] + v_{\rm visc}\,(1+\lambda_0+{\rm St}_i\lambda_1)}{\left[(1+\lambda_0)^2+\lambda_1^2\right]\left(1+{\rm St}_i^2\right)}, \tag{59}$$

where $v_{\rm P}$, the dust drift velocity due to the gas being pressure-supported, is

$$v_{\rm P} = \frac{1}{\rho_g\Omega_k}\frac{\partial P}{\partial R}, \tag{60}$$

and $v_{\rm visc}$, the gas radial velocity due to viscous spreading, is

$$v_{\rm visc} = \left[R\rho_g\frac{\partial}{\partial R}\left(R^2\Omega_k\right)\right]^{-1}\frac{\partial}{\partial R}\left(\eta R^3\frac{\partial\Omega_k}{\partial R}\right), \tag{61}$$

with $\eta = \nu\rho_g = \alpha c_s H\rho_g$ (where α is the Shakura & Sunyaev (1973) viscosity parameter) and λ_k is given by

$$\lambda_k = \sum_i \frac{{\rm St}_i^k}{1+{\rm St}_i^2}\epsilon_i. \tag{62}$$

We used equations (58) and (59) to validate our numerical method for the radial drift test.

We set up a 3D, locally isothermal protoplanetary disc around a star of 1 $M_\odot$. We used 10 dust species logarithmically distributed

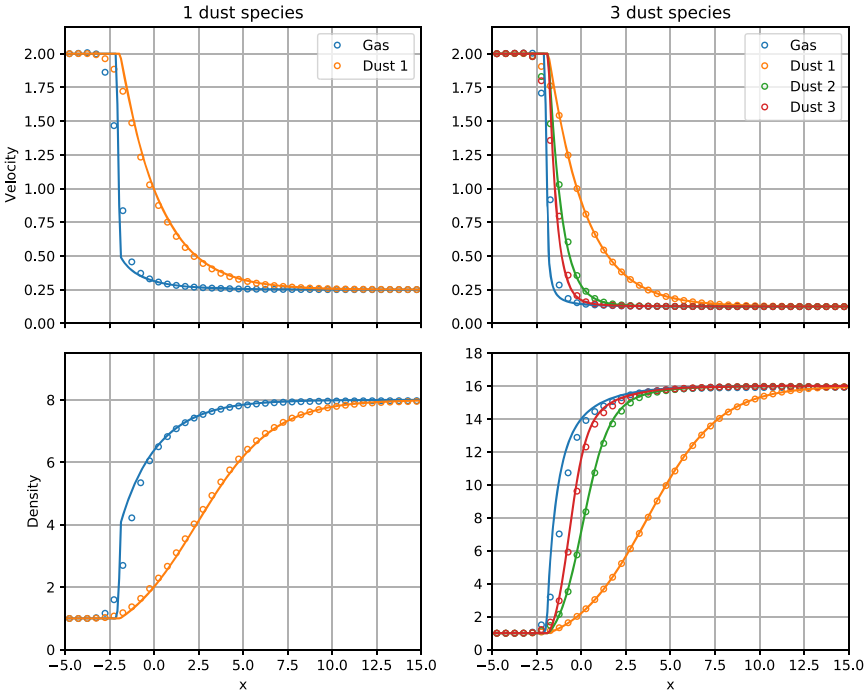

Figure 6. Dusty shock numerical test showing the velocity (top) and the density (bottom) at time $t = 300$. The left figures have gas (in blue) and one dust species; the right figures have gas (blue) and three dust species. The open circles represent the results from the PHANTOM simulation. The solid lines represent the analytical solution from Benítez-Llambay et al. (2019).

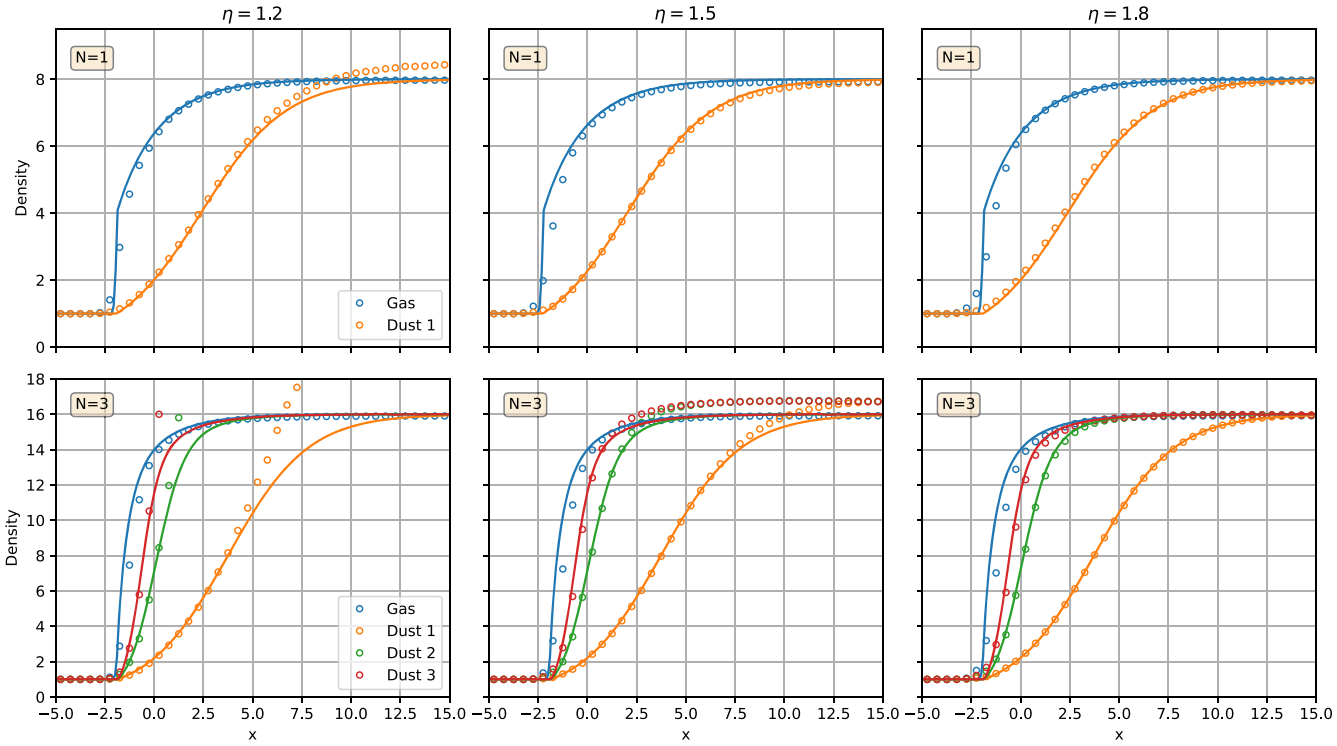

Figure 7. The effect of η in the dusty shock test problem. The lines and the markers are the same as used in Fig. 6. From left to right: $\eta = 1.2, 1.5, 1.8$, corresponding to $\overline{N}_{\rm neigh} = 195, 381, 660$. For the single dust species case, we require 381 neighbours. For the three dust species case, we require 660 neighbours.

in size from 1 to 10^4 cm. The gas mass was 0.05 $M_\odot$ and the total dust-to-gas ratio was 0.5. The dust sub-disc mass for each species scaled with the grain size. We used 10^6 gas particles and 10^6 dust particles with 10^5 per species. We used a dust grain material density of 3 g cm^{-3}. The disc extends from 1 to 150 au. The radial profile of the surface density was given by $\Sigma(R) \propto R^{-1}$. The radial profile for the gas temperature was given by $T(R) \propto R^{-0.5}$ with the aspect ratio $H/R = 0.05$ at $R = 1$ au. We used α-disc viscosity (section 3.3.4, Price

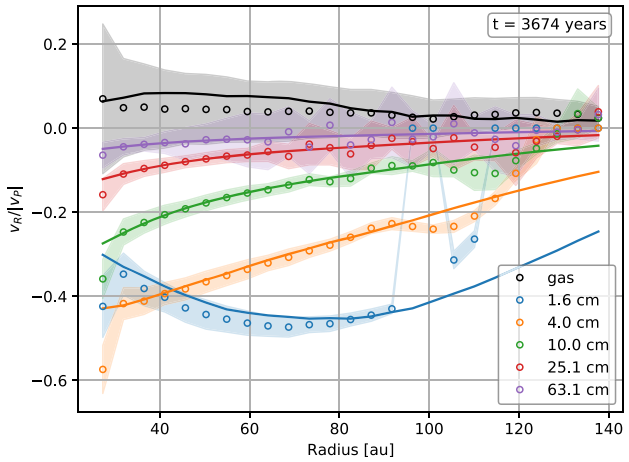

Figure 8. Azimuthally averaged radial drift velocity profiles for gas (black) and five dust species (other colours). The circle markers represent the drift velocities measured directly on the particles with shading indicating the standard deviation from radial binning. The solid line corresponds to the analytical solution from Dipierro et al. (2018). The numerical and analytical solutions agree within the variation due to binning. The error in the 1.6 cm and 4.0 cm grains for radius $\gtrsim$90 au is due to the depletion of those grains at those radii.

et al. 2018a) with an artificial viscosity parameter $\alpha_{\rm AV} = 0.74$. We set the initial radial velocities to zero. We set the orbital velocities to account for the pressure gradient (section 3.3.2, Price et al. 2018a). Initially, the dust sub-discs are co-located with the gas disc. We used individual time-stepping (section 2.3.4, Price et al. 2018a).

After evolving the disc for 3674 yr, we binned the particles into 25 equally spaced radial bins between 25 and 140 au. For the analysis, we considered only particles within 0.05 times the gas scale height of the mid-plane. The Stokes number is exponentially dependent on the height above the mid-plane ($\mathrm{St_i} \sim \rho_g^{-1} \sim e^{z^2}$). Averaging, within a radial bin, by including particles above the mid-plane ($\gtrsim 0.05\,H_{\rm g}$) produces a poor estimate of the mid-plane Stokes number. We computed the mass-weighted average of the radial velocities in the each annular cylinder for the gas and each dust species. To compare with the analytical solution (equations 58 and 59), we computed each of the terms (equations 60–62) on the radial bins. We computed the gradient terms using a second-order finite difference approximation.

Fig. 8 shows this comparison of the radial drift velocities for the five smallest dust species. The drift velocities are scaled by $v_{\rm P}$. We omit grains larger than 63.1 cm as they are consistent with zero radial drift. The shading represents the standard deviation from the binning procedure. The solid lines represent the drift velocities computed from equations (58) and (59). We see that for most of the radial extent of the disc the drift velocities match to within the error introduced by binning. The deviation for the 1.6 and 4 cm grains for radius $\gtrsim$90 au is due to depletion of those grains via radial drift.

4 DISCUSSION

In deriving our method, we made no assumptions on the size of the dust grains. This is unlike the method described in Hutchison et al. (2018) that makes the terminal velocity approximation, appropriate for small, well-coupled grains (Youdin & Goodman 2005).

However, we use an explicit time-stepping scheme (Price et al. 2018a). In addition to the usual Courant–Friedrichs–Lewy (CFL) time-step constraint (Courant, Friedrichs & Lewy 1928), which in SPH form is $\Delta t_{\rm CFL} < C_{\rm Cour} h/c_{\rm s}$ (Price et al. 2018a), there is an extra constraint given in equation (29). This restricts the minimum stopping time of grains that can be simulated. To get an estimate on this restriction we compare this constraint with the CFL constraint. If we require that the stopping time constrained time-step is less restrictive than the CFL constraint, then we get that

$$t_{s_i} > \frac{C_{\rm Cour} h(1-\varepsilon)}{C_{\rm drag} c_{\rm s}}. \tag{63}$$

The parameters c_s and ε are physical parameters set by the problem of interest. Whereas $C_{\rm Cour} = 0.3$, $C_{\rm drag} = 0.9$, and h are numerical parameters.

Considering protoplanetary discs, converting this into an inequality for the mid-plane Stokes number St_i we get

$$\mathrm{St}_i > \frac{C_{\rm Cour}}{C_{\rm drag}}(1-\varepsilon)\frac{h}{H}, \tag{64}$$

where H is the gas disc scale height. Using values of $h/H \approx 0.5$ and $\varepsilon \approx 0.1$ we find a minimum Stokes number, such that the time-step is unconstrained compared with the CFL condition, of $\mathrm{St}_i \gtrsim 0.1$. Note that the numerical resolution is inversely proportional to h. So, as the resolution increases this restriction is loosened. However, as the resolution increases the CFL time-step decreases.

The Stokes number is linearly proportional to the grain size (in the Epstein regime). So, this constraint on the Stokes number provides a constraint on the dust grain size; one that is dependent on the disc parameters too. Considering a disc with surface density $\Sigma \approx 1\ \mathrm{g\,cm^{-3}}$ and effective grain size $\varrho_{\rm eff} = 3\ \mathrm{g\,cm^{-3}}$ we find that the minimum grain size is approximately 0.2 mm. Note that this is *not* a minimum grain size that can be represented. Using smaller grains is merely inefficient given the explicit time-stepping scheme. The single fluid method is more efficient for these smaller grains, which satisfy the terminal velocity approximation. Cuello et al. (2019) show that the two methods overlap and give the same results. Using the single fluid method for small grains negates the need to implement an implicit time-stepping scheme as in, e.g. Lorén-Aguilar & Bate (2014), Lorén-Aguilar & Bate (2015).

The method requires storing an extra set of particles per dust species. For each particle, we store the position, smoothing length, and velocity, in total requiring seven 64-bit floating point numbers per particle. This is in contrast to the mixture method. In that method there is only a single set of particles (representing the mixture) and for each dust species an additional four 64-bit floating point numbers are required: one for the dust fraction, and three for the velocity differential (Hutchison et al. 2018). So, it seems that the method described here is more expensive in memory and storage requirements than Hutchison et al. (2018). However, this is not so. In practice, we use fewer dust SPH particles than gas; see, for example, Dipierro et al. (2015), Mentiplay et al. (2019), and Calcino et al. (2019). This is to prevent the dust from becoming trapped under the gas resolution scale (Laibe & Price 2012a). In either case, the additional memory and storage requirement is not prohibitive.

We represent each dust species as a pressureless fluid that interacts with gas via the drag force and with massive objects such as stars and planets (represented by sink particles) by the gravitational force. The gas, in contrast, has a non-zero pressure. The pressure gradient force leads to a rearrangement of particles into a regular glass-like lattice (Monaghan 2005) that minimizes the Lagrangian of the system of particles (Price 2012). So, if the gas particles are initialized in a 'pathological' arrangement, e.g. such that particles are almost on top of each other or randomized, they will rearrange into a quasi-regular lattice. This rearrangement leads to an improved density estimate

(Price 2012). The lack of rearranging due to the lack of a pressure gradient force in the dust can lead to noisy density estimates.

In calculating the density, we sum over neighbours of the same type. So, the gas and each dust species has a smoothing length per particle independent of each other species. In PHANTOM, the smoothing length proportionality factor η is constant. This means that the mean number of neighbours $\overline{N}_{\rm neigh}$ is the same for both the gas and dust. Given that the dust particle arrangement does not re-mesh, unlike the gas, using a larger number of neighbours may improve the density estimate for the dust. One possible approach, not explored in this study, would be to set η independently for the gas and dust. The dusty shock test (Section 3.3) provides some evidence for this. In that test, the gas density was accurate for $\eta = 1.2$. However, the dust density required $\eta = 1.8$ in the three dust species case.

An alternative approach would be to provide a pressure gradient force for the dust. This would provide for a rearrangement of particles to improve the density estimates and reduce artificial clumping of dust. Such a force would necessarily be a short range one. It is not clear at what distance it should activate. Any such prescription would be a sub-grid model and resolution dependent.

In the limit of small drag coefficient, or large stopping time, our scheme reduces to an N-body integrator, which preserves the orbital parameters exactly. As the method is Lagrangian, we can track particles throughout time. This allows for coupling with, for example, chemistry codes that require knowledge of the thermal history of the dust.

5 CONCLUSIONS

We have derived an SPH numerical scheme to model a dust and gas mixture using a separate set of SPH particles per species. The method includes a drag force coupling between the gas and each dust species that conserves momentum. Thus, the method captures the full effects of backreaction between the gas and dust. This method can be applied to any distribution of dust grain sizes. It is not restricted to grain sizes such that the terminal velocity approximation holds. Although given that it uses an explicit time-stepping scheme, it becomes inefficient for grain sizes with small Stokes number, i.e. $\lesssim$0.05.

We have implemented this method in the SPH code PHANTOM. We have demonstrated that the method is accurate by testing it on four test problems with analytical solutions: a dusty box, to test the drag coupling and time-stepping in the absence of spatial gradients; a dusty wave, to test those factors with spatial gradients in a linear regime; a dusty shock, to test those factors in a highly non-linear regime; and a radial drift test to test the method is the context of a global 3D protoplanetary disc model. In all cases, we show the method is accurate.

We suggest that dust particles may require a larger number of particle neighbours in computing SPH sums than the gas. This is due to the lack of interparticle forces, i.e. dust is pressureless fluid and does not rearrange into a glassy structure like the gas does. Dust can numerically clump resulting in artificial high-density regions. Using a greater number of particle neighbours leads to a smoother density field. This may reduce the performance degrading effect of high-density dust clumps on the time-step.

ACKNOWLEDGEMENTS

DM is funded by a Research Training Program Stipend from the Australian government. We acknowledge Australian Research Council funding via DP180104235, FT130100034, and FT170100040. GL acknowledges funding from the European Union's Horizon 2020 research and innovation program under the H2020 Marie Skłodowska-Curie Actions grant agreement No. 823823 and ERC CoG project PODCAST No. 864965. We used OzStar, funded by Swinburne University of Technology and the Australian government, for computation. DP thanks Pablo Benítez-Llambay for useful discussions at the Great Barriers in Planet Formation conference, 2019. We used PHANTOM to perform the numerical simulations (Price et al. 2018a). We used PLONK for analysis and visualization of PHANTOM data (Mentiplay 2019). We also used the following PYTHON packages and tools: NUMPY (Oliphant 2006; van der Walt, Colbert & Varoquaux 2011), H5PY (Collette 2013), MATPLOTLIB (Hunter 2007), PANDAS (McKinney 2010), IPYTHON (Perez & Granger 2007), and JUPYTER (Kluyver et al. 2016).

DATA AVAILABILITY

The data underlying this article can be reproduced following instructions in a file `README.md` in the repository 'multigrain' (available on GitHub at https://github.com/dmentipl/multigrain and archived on Figshare at https://doi.org/10.6084/m9.figshare.13076435). This repository contains PYTHON code used to set up the tests and generate data, analyse the output data from the tests, and produce the figures of the manuscript. It contains a file `environment.yml` that can be used – along with conda, a cross-platform, software package manager – to set up a computing environment with the required software dependencies. We used the PHANTOM version with git hash `64dbd2b1` with some patches described in the 'multigrain' repository.

REFERENCES

ALMA Partnership, 2015, ApJ, 808, L3
Andrews S. M. et al., 2016, ApJ, 820, L40
Andrews S. M., 2015, PASP, 127, 961
Ayliffe B. A., Laibe G., Price D. J., Bate M. R., 2012, MNRAS, 423, 1450
Bai X.-N., Stone J. M., 2010a, ApJS, 190, 297
Bai X.-N., Stone J. M., 2010b, ApJ, 722, 1437
Ballabio G., Dipierro G., Veronesi B., Lodato G., Hutchison M., Laibe G., Price D. J., 2018, MNRAS, 477, 2766
Benítez-Llambay P., Krapp L., Pessah M. E., 2019, ApJS, 241, 25
Calcino J., Price D. J., Pinte C., van der Marel N., Ragusa E., Dipierro G., Cuello N., Christiaens V., 2019, MNRAS, 490, 2579
Casassus S. et al., 2015, ApJ, 812, 126
Collette A., 2013, Python and HDF5, O'Reilly Media
Courant R., Friedrichs K., Lewy H., 1928, Math. Ann., 100, 32
Cuello N. et al., 2019, MNRAS, 483, 4114
Dipierro G., Laibe G., 2017, MNRAS, 469, 1932
Dipierro G., Price D., Laibe G., Hirsh K., Cerioli A., Lodato G., 2015, MNRAS, 453, L73
Dipierro G., Laibe G., Alexander R., Hutchison M., 2018, MNRAS, 479, 4187
Epstein P. S., 1924, Phys. Rev., 23, 710
Gonzalez J. F., Laibe G., Maddison S. T., 2017, MNRAS, 467, 1984
Haworth T. J. et al., 2016, Publ. Astron. Soc. Aust., 33, e053
Huang J. et al., 2018, ApJ, 852, 122
Hunter J. D., 2007, Comput. Sci. Eng., 9, 90
Hutchison M., Price D. J., Laibe G., 2018, MNRAS, 476, 2186
Kanagawa K. D., Ueda T., Muto T., Okuzumi S., 2017, ApJ, 844, 142
Kluyver T. et al., 2016, in Loizides F., Schmidt B., eds, Positioning and Power in Academic Publishing: Players, Agents and Agendas. IOS Press, Netherlands, p. 87
Kwok S., 1975, ApJ, 198, 583
Laibe G., Price D. J., 2011, MNRAS, 418, 1491
Laibe G., Price D. J., 2012a, MNRAS, 420, 2345

Laibe G., Price D. J., 2012b, MNRAS, 420, 2365
Laibe G., Price D. J., 2014a, MNRAS, 440, 2136
Laibe G., Price D. J., 2014b, MNRAS, 440, 2147
Laibe G., Price D. J., 2014c, MNRAS, 444, 1940
Lebreuilly U., Commerçon B., Laibe G., 2019, A&A, 626, A96
Lehmann A., Wardle M., 2018, MNRAS, 476, 3185
Li Y.-P. et al., 2019, ApJ, 878, 39
Lorén-Aguilar P., Bate M. R., 2014, MNRAS, 443, 927
Lorén-Aguilar P., Bate M. R., 2015, MNRAS, 454, 4114
McKinney W., 2010, in van der Walt S., Millman J., eds, Proceedings of the 9th Python in Science Conference. SciPy, Austin, Texas, US, p. 51
Mentiplay D., 2019, J. Open Source Softw., 4, 1884
Mentiplay D., Price D. J., Pinte C., 2019, MNRAS, 484, L130
Monaghan J. J., 1992, ARA&A, 30, 543
Monaghan J. J., 1997, J. Comput. Phys., 138, 801
Monaghan J. J., 2005, Rep. Prog. Phys., 68, 1703
Monaghan J. J., Kocharyan A., 1995, Comput. Phys. Commun., 87, 225
Nakagawa Y., Sekiya M., Hayashi C., 1986, Icarus, 67, 375
Oliphant T. E., 2006, A Guide to NumPy. Trelgol Publishing, USA
Perez F., Granger B. E., 2007, Comput. Sci. Eng., 9, 21
Pinte C., Dent W. R. F., Ménard F., Hales A., Hill T., Cortes P., de Gregorio-Monsalvo I., 2016, ApJ, 816, 25
Poblete P. P., Cuello N., Cuadra J., 2019, MNRAS, 489, 2204
Porth O., Xia C., Hendrix T., Moschou S. P., Keppens R., 2014, ApJS, 214, 4
Price D. J. et al., 2018a, Publ. Astron. Soc. Aust., 35, e031
Price D. J. et al., 2018b, MNRAS, 477, 1270
Price D. J., 2012, J. Comput. Phys., 231, 759
Price D. J., Laibe G., 2015, MNRAS, 451, 813
Price D. J., Laibe G., 2020, MNRAS, 495, 3929
Shakura N. I., Sunyaev R. A., 1973, A&A, 500, 33
Stoyanovskaya O. P., Glushko T. A., Snytnikov N. V., Snytnikov V. N., 2018, Astron. Comput., 25, 25
Takeuchi T., Lin D. N. C., 2002, ApJ, 581, 1344
Tricco T. S., Price D. J., Laibe G., 2017, MNRAS, 471, L52
van der Marel N., Pinilla P., Tobin J., van Kempen T., Andrews S., Ricci L., Birnstiel T., 2015, ApJ, 810, L7
van der Walt S., Colbert S. C., Varoquaux G., 2011, Comput. Sci. Eng., 13, 22
Weidenschilling S. J., 1977, MNRAS, 180, 57
Youdin A. N., Goodman J., 2005, ApJ, 620, 459

This paper has been typeset from a TEX/LATEX file prepared by the author.